

Microscopic deformation mechanism of a $\text{Ti}_{66.1}\text{Nb}_{13.9}\text{Ni}_{4.8}\text{Cu}_8\text{Sn}_{7.2}$ nanostructure–dendrite composite

K.B. Kim ^{a,*}, J. Das ^{b,c}, W. Xu ^{b,d}, Z.F. Zhang ^e, J. Eckert ^b

^a Department of Advanced Materials Engineering, Sejong University, 98 Gunja-dong, Gwnagjin-gu, Seoul 143-747, Republic of Korea

^b FG Physikalische Metallkunde, FB 11 Material- und Geowissenschaften, Technische Universität Darmstadt, Petersenstraße 23, D-64287 Darmstadt, Germany

^c Leibniz-Institut für Festkörper- und Werkstofforschung, Dresden, Helmholtzstraße 20, D-01069 Dresden, Germany

^d Department of Mechanical & Manufacturing Engineering, The University of Melbourne, Parkville, Melbourne VIC 3010, Australia

^e Shenyang National Laboratory for Materials Science, Institute of Metal Research, Chinese Academy of Sciences, 72 Wenhua Road, Shenhe District, Shenyang 110016, China

Received 18 November 2005; received in revised form 6 March 2006; accepted 1 April 2006

Available online 27 June 2006

Abstract

Systematic investigations of the microstructural changes upon compression have been performed in order to elucidate the microscopic deformation mechanisms of the high-strength and ductile $\text{Ti}_{66.1}\text{Nb}_{13.9}\text{Ni}_{4.8}\text{Cu}_8\text{Sn}_{7.2}$ nanostructure–dendrite composite. After 8% deformation, a rotation of β -Ti dendrites is observed during the interaction of slip and shear bands. This rotation leads to the formation of new slip bands in the dendrites. The β -Ti dendrites locally transform into ω phase during the interaction between the newly and the previously formed slip bands. The rotation of the dendrites causes local volume changes at the interfacial areas between the dendrites and the matrix, consisting of a mixture of hexagonal close-packed α -Ti and body-centered tetragonal Ti_2Cu phases. This induces a rotational stress into the nanostructured matrix. After further deformation up to 25%, the shear bands penetrate the dendrite/matrix interfaces, producing extra interfaces. The nanostructured matrix exhibits a sandwiched microstructure in order to accommodate effectively the shear strains. These results suggest that structural coherency of the dendrite/matrix interfaces is important for controlling both the strength and the ductility of the nanostructure–dendrite composite.

© 2006 Acta Materialia Inc. Published by Elsevier Ltd. All rights reserved.

Keywords: Plastic deformation; Compression test; Transmission electron microscopy; Phase transformation; Nanocomposite

1. Introduction

Nanostructure–dendrite composites have been recently developed in a series of Ti-based [1–5] and Zr-based [6,7] multicomponent alloys. These alloys exhibit a strength of more than 2 GPa and a ductility of more than 15% at room temperature, showing superior plastic deformability compared to monolithic nanostructured metallic alloys. So far, several investigations have been reported on the deformation and the fracture behavior to understand the mech-

anisms responsible for the high strength and ductility of nanostructure–dendrite composites [8–10]. Measurement of the fracture angles has revealed that alloys with higher volume fraction of dendrites exhibit higher fracture angles [10]. Based on such measurements, the deformation of the composites has been suggested to occur by a rotation mechanism triggered by the interaction between primary and secondary shear bands followed by dendrite peeling-off from the matrix [8]. It is clear that the volume fractions of the dendrites and the nanostructured matrix are crucial parameters that determine the overall strength and ductility. However, the deformation behavior of nanostructure–dendrite composites has so far mostly been described on the basis of a macroscopic analysis of fracture. Consequently,

* Corresponding author. Tel.: +49 6151 163512; fax: +49 6151 165557.
E-mail addresses: k.b.kim@phm.tu-darmstadt.de, kbkim@sejong.ac.kr (K.B. Kim).

it is necessary to investigate the deformation behavior incorporating possible microstructural changes upon different degrees of deformation in order finally to derive a microscopic model-based understanding of the processes governing the mechanical properties of this new class of materials.

Recently, a microstructural investigation of the deformed $\text{Ti}_{62}\text{Nb}_8\text{Ni}_{12}\text{Cu}_{14}\text{Sn}_4$ nanostructure–dendrite composite revealed that work hardening occurred by the formation of slip bands in the dendrites at the initial stage of plastic deformation (5% strain) [11]. With increasing deformation up to 13.5%, the formation of shear bands, which were initiated at the interfaces between the dendrites and the nanostructured matrix, was observed. These results suggest that the work-hardened dendrites can resist the propagation of the shear bands during further deformation. After 22.5% strain, the propagation and interaction of the shear bands are dominant, resulting in a pronounced plateau in the stress–strain curve [11]. This plateau region indicates that the propagation and interaction of the shear bands cause no further work hardening in this composite [11].

In contrast, the compressive stress–strain curve for the $\text{Ti}_{66.1}\text{Nb}_{13.9}\text{Ni}_{4.8}\text{Cu}_8\text{Sn}_{7.2}$ nanostructure–dendrite composite exhibited a continuous stress increase with increasing strain, pointing to continuous work hardening until failure [3,12]. More recently, investigations of the highly deformed (25% strain) $\text{Ti}_{66.1}\text{Nb}_{13.9}\text{Ni}_{4.8}\text{Cu}_8\text{Sn}_{7.2}$ revealed that the propagation and interaction of shear bands in the dendrites [13] induced local amorphization and distortion of the supersaturated dendrites [14]. Furthermore, there is a heterogeneous distribution of shear strains according to the geometry of the dendrites [15]. So far, there are no clear microscopic mechanisms that could fully explain the deformation behavior of the $\text{Ti}_{66.1}\text{Nb}_{13.9}\text{Ni}_{4.8}\text{Cu}_8\text{Sn}_{7.2}$ nanostructure–dendrite composite.

In the present investigation, the microstructural changes of the $\text{Ti}_{66.1}\text{Nb}_{13.9}\text{Ni}_{4.8}\text{Cu}_8\text{Sn}_{7.2}$ nanostructure–dendrite composite subjected to different amounts of deformation (8% and 25% strain, respectively) have been analyzed using transmission electron microscopy (TEM) in order to understand the microscopic deformation mechanisms of this high-strength and ductile material.

2. Experimental

Master alloy ingots with a nominal composition of $\text{Ti}_{66.1}\text{Nb}_{13.9}\text{Ni}_{4.8}\text{Cu}_8\text{Sn}_{7.2}$ were prepared by arc-melting a mixture of Ti, Cu, Ni, Sn, and Nb metals (purity 99.99%) using a water-cooled copper hearth under an argon atmosphere. The master alloy ingots were remelted several times until a homogenous melt was achieved and cooled at a slow rate. Cast rods were solidified through cold crucible casting (10 mm diameter, 180 mm length) and characterized by X-ray diffraction (XRD) using a Philips D500 diffractometer with Cu $K\alpha$ radiation. The microstructure and the phases present in the alloy were examined using scanning electron

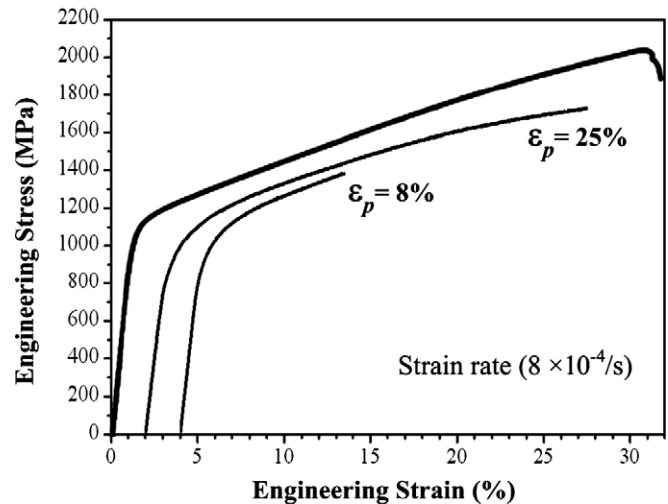


Fig. 1. Typical compressive stress–strain curves of the $\text{Ti}_{66.1}\text{Nb}_{13.9}\text{Ni}_{4.8}\text{Cu}_8\text{Sn}_{7.2}$ nanostructure–dendrite composite. The tests were stopped at different strains ($\epsilon_p = 8\%$ and 25%) for SEM and TEM observation.

microscopy (SEM; Zeiss 962), high-resolution SEM (Philips XL 30) and TEM (Philips CM 20).

Bar-shaped compression specimens were prepared by machining the as-cast specimens to 2 mm \times 2 mm cross section and 4 mm height. The surfaces were polished and etched to observe the as-cast microstructure, also allowing for the following observation of the surface deformation morphology. The compression tests were performed using a Schenck hydraulic testing machine under quasi-static loading (strain rate of $8 \times 10^{-4} \text{ s}^{-1}$) at room temperature on two different types of specimens: samples deformed up to a plastic strain of $\epsilon_p = 8\%$ (partially deformed samples) and then unloaded; and samples deformed up to a strain of $\epsilon_p = 25\%$ (fully deformed samples) and then unloaded (cf. the stress–strain curves in Fig. 1). One specimen was compressed until fracture. After compression, the surface deformation morphology was examined using SEM.

After deformation, the cross sectional area of the deformed sample was sliced by precision cutting [15]. The detailed structural investigations of the deformed samples were performed using high-resolution TEM (HRTEM; Philips CM 20) coupled with energy-dispersive X-ray analysis (EDX; Noran). Fourier transformed patterns were obtained using a DigitalMicrograph 3.3.1 program (Gatan). The TEM samples were prepared by the conventional method of slicing and grinding, followed by ion milling (BALTECH-RES 010).

3. Results

3.1. Deformation behavior and fractography identification

Fig. 1 shows typical compressive stress–strain curves of the $\text{Ti}_{66.1}\text{Nb}_{13.9}\text{Ni}_{4.8}\text{Cu}_8\text{Sn}_{7.2}$ nanostructure–dendrite composite. The values of Young's modulus E , yield stress σ_y , yield strain ϵ_y , ultimate compression stress σ_{max} , and fracture strain ϵ_f were 58 GPa, 1024 MPa, 1.8%, 2020 MPa,

and 31.8%, respectively. The pronounced work-hardening behavior after yielding was clearly visible. In order to investigate systematically the microstructural changes upon deformation, two types of samples subjected to different amounts of plastic strain were prepared, i.e. partially deformed ($\epsilon_p = 8\%$) and fully deformed ($\epsilon_p = 25\%$) samples, as shown in Fig. 1.

Fig. 2 displays the XRD patterns of as-cast, partially deformed and fully deformed samples. All XRD patterns revealed that the predominant crystalline phase was a body-centered cubic (bcc) β -Ti solid solution (space group: Im3m) [16] with a lattice parameter of 0.332 nm, which is slightly larger than that of pure β -Ti (0.3306 nm) [16]. Comparing these data with previous reports on the lattice

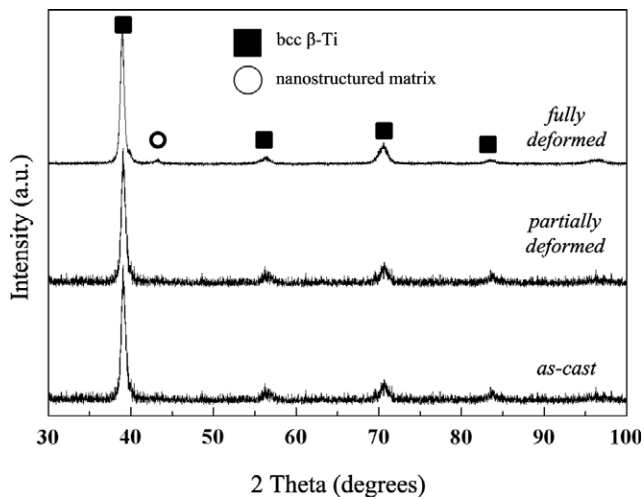


Fig. 2. XRD patterns of as-cast, partially deformed ($\epsilon_p = 8\%$) and fully deformed ($\epsilon_p = 25\%$) samples.

parameter of the β -Ti phase in $\text{Ti}_{60}\text{Ta}_{10}\text{Ni}_{12}\text{Cu}_{14}\text{Sn}_4$ [4,17] revealed that the β -Ti dendritic phase in the present alloy contained higher levels of solute. Also, the diffraction peaks from a hexagonal close-packed (hcp) α -Ti solid solution (space group: P63/mmc) and a body-centered tetragonal (bct) Ti_2Cu intermetallic compound (space group: I4/mmm) were present [13–15]. However, recent TEM investigations of a fully deformed sample revealed the occurrence of local amorphization at the shear bands in the dendrites [14], which is difficult to resolve using XRD.

Fig. 3 shows SEM secondary electron images obtained from the surfaces of the partially deformed (Fig. 3(a) and (b)) and fully deformed samples (Fig. 3(c) and (d)). Fig. 3(a) and (b) reveal the formation of fine-scale bands in the dendrites for the partially deformed sample, as marked by solid-line white arrows. The band width was approximately 200–400 nm. Usually, the fine-scale deformation bands were arrested at the interfaces between the dendrites and the matrix. This suggests that the interfaces act as a barrier for propagating the deformation through the sample. There was no preferred orientation for the fine-scale deformation bands, indicating an overall homogeneous deformation. Since the work hardening of the composite was clearly apparent in the stress–strain curve (Fig. 1), these bands were considered as slip bands that formed due to the movement of dislocations in the dendrites, similar as those previously observed in the $\text{Ti}_{62}\text{Nb}_8\text{Ni}_{12}\text{Cu}_{14}\text{Sn}_4$ composite [11]. In addition, shear bands that penetrated the dendrite/matrix interfaces were observed, as marked by the dashed arrows in Fig. 3. One interesting feature of the profuse slip bands in the dendrites is their significantly wavy nature instead of straightforward propagation when the slip bands interact with the shear bands. This suggests that the direction of the slip bands can be

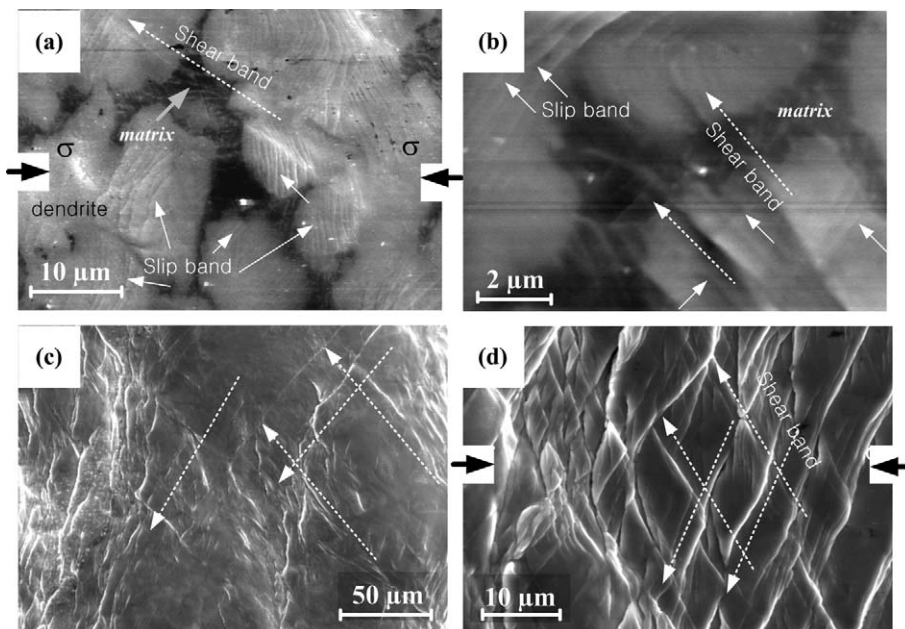


Fig. 3. SEM secondary electron images obtained from the surfaces of the partially deformed (a and b) and fully deformed (c and d) samples.

distorted by passing the shear bands. The present features of the deformation of the $\text{Ti}_{66.1}\text{Nb}_{13.9}\text{Ni}_{4.8}\text{Cu}_8\text{Sn}_{7.2}$ composite are very similar to the typical deformed microstructure at the early stage of work hardening found for the $\text{Ti}_{62}\text{Nb}_8\text{Ni}_{12}\text{Cu}_{14}\text{Sn}_4$ nanostructure–dendrite composite. The formation of both slip and shear bands was also observed at the early stage of deformation of $\text{Ti}_{62}\text{Nb}_8\text{Ni}_{12}\text{Cu}_{14}\text{Sn}_4$ [11]. However, in the present investigation, it is very difficult to identify the nanostructured matrix using SEM due to its small volume fraction (10–15 vol.%), as observed from the as-cast microstructure (not shown here).

Upon further compression to a strain of 25% (fully deformed sample), shear bands were frequently observed throughout the sample, as shown in Fig. 3(c) and (d). A homogeneous propagation and interaction of the shear bands was visible on the surface, reflecting that there was no significant shear band localization. Moreover, shear bands were interrupted by interaction and formed steps, indicating the occurrence of shear band multiplication at this strain level. The shear bands were found to pass through the sample at an angle of 55–60° with the compression direction. This suggests that the work hardening visible in the stress–strain curve (Fig. 1) is mainly correlated with the formation of the slip bands in the dendrites. On further increasing the strain up to 25%, the propagation and multiplication of shear bands were dominant rather than the formation of slip bands. As shown in Fig. 1, there was a continuous increase of the stress with increasing strain up to failure, indicating continuous work hardening even at a high strain level.

In general, it is well known that the propagation and multiplication of shear bands do not lead to work hardening but result in a plateau stress–strain curve, similar to that previously observed for the $\text{Ti}_{62}\text{Nb}_8\text{Ni}_{12}\text{Cu}_{14}\text{Sn}_4$ nanostructure–dendrite composite [11]. Consequently, a different deformation mechanism may be operative for the present $\text{Ti}_{66.1}\text{Nb}_{13.9}\text{Ni}_{4.8}\text{Cu}_8\text{Sn}_{7.2}$.

3.2. TEM identification on the deformed β -Ti dendrites

Fig. 4 shows TEM bright-field images (Fig. 4(a) and (b)), a dark-field image (Fig. 4(c)) and the corresponding selected area diffraction pattern (Fig. 4(d)) of the dendrites for the partially deformed sample. Fig. 4(a) reveals a strained microstructure for both the dendrite and the nanostructured matrix. The interface between the dendrite and the nanostructured matrix was uneven, as marked by the arrows, suggesting that the slip bands in the dendrite were accommodated at the interface. The step spacing was around 200–300 nm. Moreover, shear bands passed through the interfaces, generating strongly strained contrast, as shown in Fig. 4(a). By comparing the thickness contrast between the slip and the shear bands, one can deduce that the shear bands involve much higher strains than the slip bands. Fig. 4(b) reveals the detailed morphology of the shear bands in the dendrite. The propagation of the shear bands was arrested inside the dendrites with very

strong strained contrast, as marked by a circle in Fig. 4(b). The strained contrast along the shear band gradually broadened from the interfacial area between the dendrite and the nanostructured matrix towards the center of the dendrite. This suggests that the shear bands are initiated at the interface. The TEM bright-field image in the inset of Fig. 4(b) reveals two specific dislocations, marked by 1 and 2. The dislocation marked by 1 was clearly arrested by the shear bands, while the dislocation marked by 2 crossed the shear band at an angle of $\sim 30^\circ$. This suggests that the propagation of the slip bands, i.e. those marked by 1 and 2, occurs at different times. The slip bands marked by 1, i.e. previously formed slip bands, form first and interact with the shear bands. Afterwards the slip bands marked by 2, i.e. newly formed slip bands, pass through the dendrites. The interaction between the slip and shear bands may be related to the macroscopic wavy nature of the slip bands due to extensive interaction, as shown in Fig. 3(a) and (b). The TEM dark-field image in Fig. 4(c) shows the detailed microstructure of the dendrite near the dendrite/matrix interface. From the contrast, one can distinguish two different slip directions at an angle of $\sim 30^\circ$, together with a discontinuous plate-like morphology in the dendrites. The plate-like areas were 20–50 nm wide and 40–150 nm long. The selected area diffraction pattern in Fig. 4(d) obtained from the dendrite corresponded to the [3–11] zone axis of the β -Ti phase. In addition, from Fig. 4(d) a disordered ω phase was confirmed to be present inside the β phase, as revealed from the broadening of the diffraction spots as well as the formation of diffuse streaks [18,19], characteristic of the presence of ω phase. This indicated that the propagation and interaction of the slip bands in the dendrite of the partially deformed sample led to the formation of the plate-like ω phase.

Fig. 5 shows TEM bright-field images (Fig. 5(a) and (b)) and the corresponding selected area diffraction patterns (Fig. 5(c) and (d)) of the dendrites for the fully deformed sample. The overall microstructure in Fig. 5(a) reveals a homogeneous distribution of shear bands in the dendrites. Shear bands were also formed perpendicularly, indicating shear band multiplication in the dendrites. The spacing of the shear bands was approximately 150–250 nm. One of the shear bands was disrupted and formed steps in the dendrite when intersected by the other shear bands (Fig. 5(a)). The morphology of the dendrite/matrix interface was stepped parallel to the direction of the shear banding. The spacing of 80–200 nm for the stepped interface was similar to that of the shear bands. This indicates that the shear bands penetrate the interfaces during their propagation. By forming the stepped interfaces, an extra interfacial area was produced in order to accommodate the shear strain. Apparently, the strain generated by the shear bands can be released during the interaction with the interfaces between the dendrites and the nanostructured matrix. A more detailed TEM dark-field image of the shear bands in a dendrite obtained at higher magnification is shown in Fig. 5(b). The strained contrast indicated that the

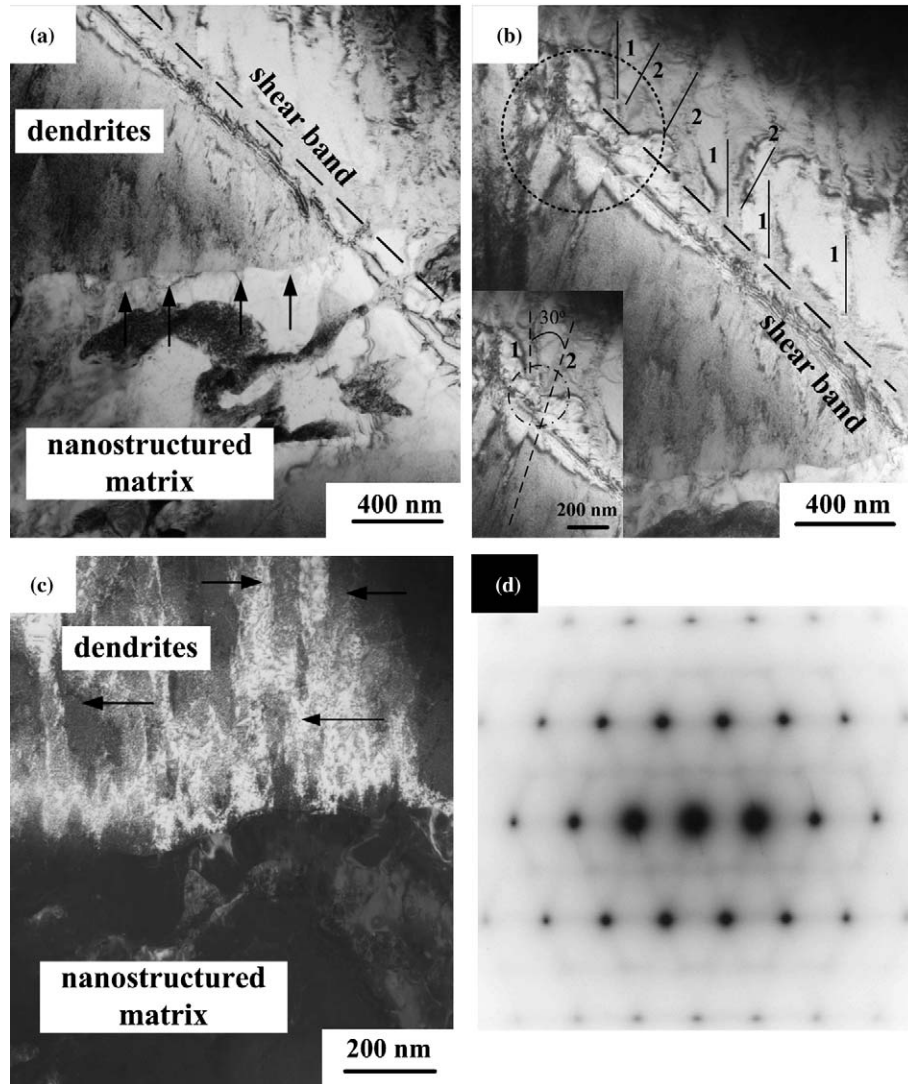


Fig. 4. TEM bright-field images (a and b), dark-field image (c) and the corresponding selected area diffraction pattern (d) of the dendrites of the partially deformed sample.

dendrites were strained by the propagation and intersection of the shear bands. In particular, a triangle-shaped contrast was often observed at the edge of the interaction region between the shear bands (marked by black-colored stars in Fig. 5(b)). Also, one can also observe moiré fringes at the edge of the interaction regions between the shear bands (marked by two white-colored stars in Fig. 5(b)), which points to local translational and rotational changes of the lattice fringes [20]. The corresponding selected area diffraction patterns in Fig. 5(c) and (d) were identified as the [1 1 1] and [1 0 0] zone axis of the bcc β -Ti dendrites, as determined by tilting the specimen ($\sim 9^\circ$). Since there was no clear extra diffraction intensity from the dendrites, they were considered as mostly single-phase bcc β -Ti.

Fig. 6 shows HRTEM images (Fig. 6(a) and (b)) and the Fourier transformed patterns (Fig. 6(c)–(f)) from a dendrite of the fully deformed sample, i.e. from the apex region of the shear band. Besides the lattice fringes of the bcc β -Ti dendrite, typical amorphous-like and distorted/disordered

lattice fringes coexisted in regions A and B, as indicated in Fig. 6(a). The distorted/disordered lattice fringes exhibited a rather continuous orientation with the lattice fringes of the bcc β -Ti dendrite. The HRTEM images in Fig. 6(b) were obtained from the [1 1 3] zone axis of the bcc β -Ti phase in order to investigate the lattice distortions in the moiré fringes observed in Fig. 5(b). The direction of the moiré fringes does not simply follow a certain direction, suggesting alternate directional changes of the lattice distortions. It is assumed that the moiré fringes are formed not only by translation but also by a mixture of translation and rotation [14]. The Fourier transformed pattern in Fig. 6(c) corresponding to the amorphous-like region A in Fig. 6(a) presented no distinguishable diffraction intensity. However, there was additional diffraction with hexagonal symmetry corresponding to the threefold symmetrical trace of the typical [1 1 1] zone axis of the bcc β -Ti phase. This suggests that the local amorphous phase (region A in Fig. 6(a)) may not have a fully random atomic arrangement

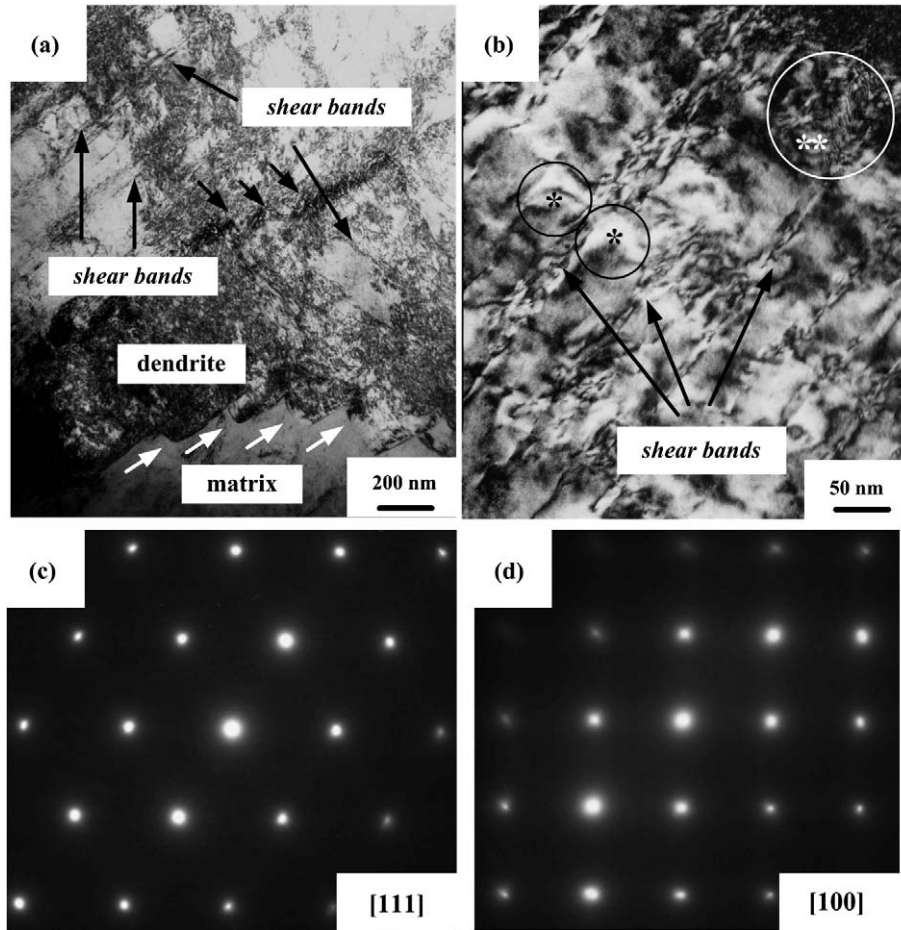


Fig. 5. TEM bright-field images (a and b) and the corresponding selected area diffraction patterns (c and d) of the dendrites of the fully deformed sample.

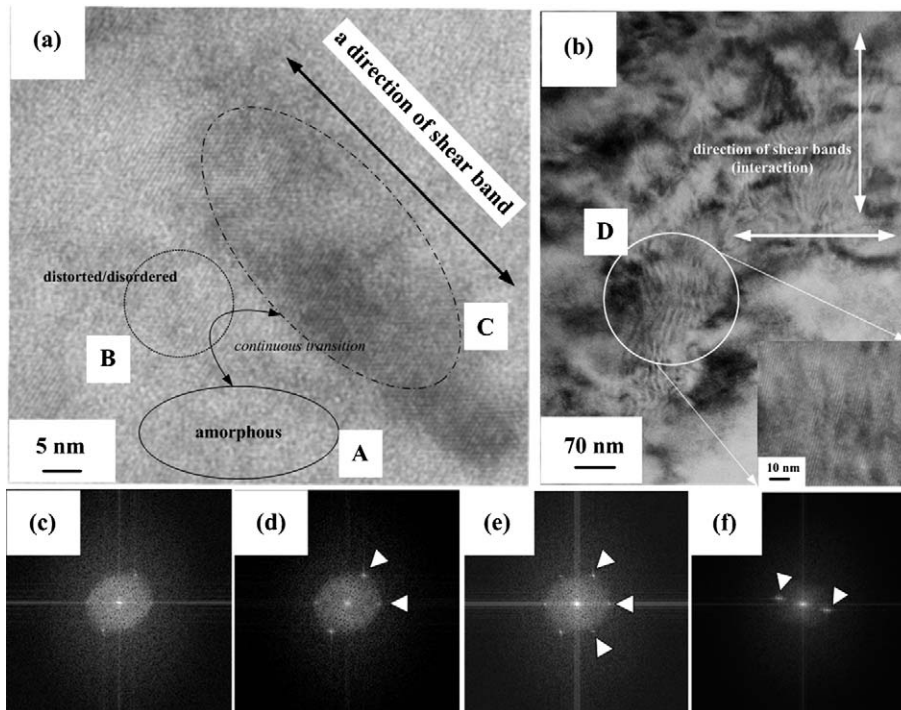


Fig. 6. HRTEM images (a and b) and the Fourier transformed patterns (c–f) from a dendrite of the fully deformed sample.

but exhibits strong atomic order. On the contrary, a weak diffraction intensity of the typical $[111]$ zone axis of the bcc β -Ti phase as marked in Fig. 6(d) was visible for the Fourier transformed pattern of the distorted/disordered lattice fringes (region B in Fig. 6(a)). Finally, Fig. 6(e) shows the clear diffraction intensity of the typical $[111]$ zone axis of the bcc β -Ti phase as obtained from region C in Fig. 6(a). These Fourier transformed diffraction patterns indicate alternate changes of the local structure along the shear bands in the dendrites of the fully deformed sample. The Fourier transformed pattern in Fig. 6(f) presents clear double diffraction intensities, suggesting the existence of significant lattice distortions in the moiré fringes. However, one cannot find amorphous-like regions at the moiré fringes, indicating that the local amorphization and the distortion of the dendrites do not occur at the intersection areas.

3.3. TEM identification on the deformed nanostructured matrix

Fig. 7 shows TEM bright-field images (Fig. 7(a)–(c)), the corresponding selected area diffraction patterns (Fig. 7(d) and (e)) and a microbeam diffraction pattern (Fig. 7(f)) for the nanostructured matrix of the partially (Fig. 7(a) and (d)) and fully deformed samples (Fig. 7(b), (c), (e), and (f)). The TEM bright-field image from the nanostructured matrix of the partially deformed sample in Fig. 7(a) reveals a large density of dislocations. High-density dislocations occurred in the phase with bright contrast whereas dislocations were often interrupted in the phase with dark contrast. The volume fraction of the bright-contrast phase was rather higher than that of the dark-contrast phase, indicating that the bright phase can encapsulate the dark

phase in the nanostructured matrix. The corresponding selected area diffraction pattern in Fig. 7(d) indicates that the diffraction peaks were well overlapped, pointing to a specific orientation relationship between two phases. Moreover, it is possible to observe a rotation of the diffraction peaks (as marked by the arrows) similar to those for textured microstructures, e.g. structures formed by equal channel angular pressing [21]. The TEM bright-field image of the fully deformed sample in Fig. 7(b) reveals a clear contrast between the two phases in the nanostructured matrix, similar as in Fig. 7(a). Most of the grains were elongated of 100–160 nm in width and 200–800 nm in length along the direction of the shear bands. Furthermore, the width of the grains agrees well with the spacing of the stepped interfaces, as shown in Fig. 5(b). The bright-field image in Fig. 7(c) was obtained from the same area of the nanostructured matrix shown in Fig. 7(b) after tilting the sample by 9° . This bright-field image reveals that the shear bands passed through the boundaries of the elongated grains, generating the stained contrast. Furthermore, moiré fringes were frequently observed at the grain boundaries. Another shear band with a perpendicular direction to the previous shear bands was significantly deflected by grain 1, losing visible contrast, as marked by the white circle 1 in Fig. 7(c). After a few layers of the sandwiched grains 1 and 2, the propagation of the shear bands was visible again, as marked by the white circle 2. A detailed investigation of the route for the propagation of the shear bands in the nanostructured matrix (Fig. 7(c)) indicated that the shear bands were reflected or detoured when the secondary shear bands met grain 1. In order to understand quantitatively the effect of the deformation on the morphology and structure of the crystalline phases in the nanostructured matrix, the corresponding selected area diffraction pattern

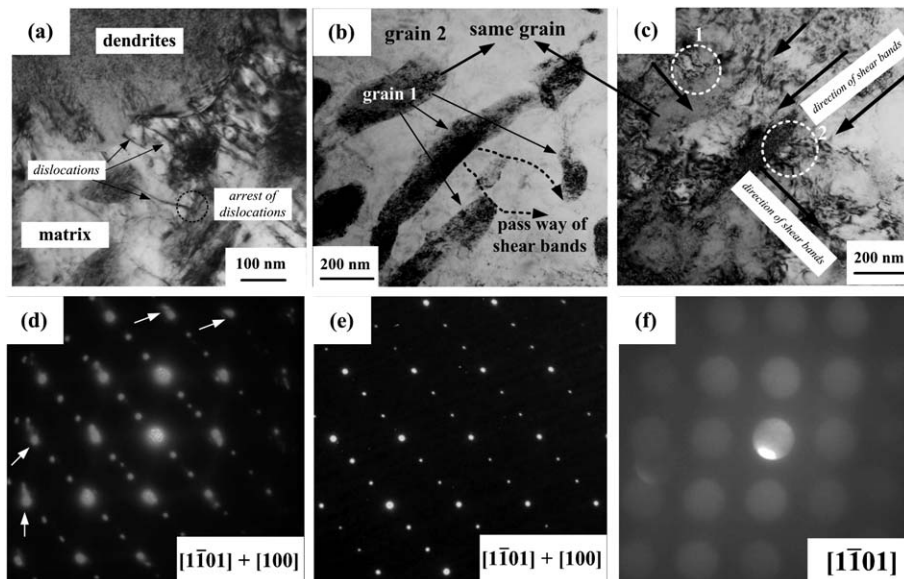


Fig. 7. TEM bright-field images (a–c), the corresponding selected area diffraction patterns (d and e) and a microbeam diffraction pattern (f) of the nanostructured matrix of the partially (a and d) and fully deformed samples (b, c, e, and f).

in Fig. 7(e) was obtained from the same zone axis as that in Fig. 7(d). When comparing Fig. 7(d) and (e), one finds that there is no rotation of the diffraction peaks in Fig. 7(e). The microbeam diffraction pattern in Fig. 7(f) from the grain of the nanostructured matrix, marked as 2 in Fig. 7(c), was identified as the $[1\bar{1}01]$ zone axis of the hcp α -Ti phase. Therefore, we can conclude that the selected area diffraction patterns in Fig. 7(d) and (e) from both grains 1 and 2 of the nanostructured matrix correspond to a combination of the $[1\bar{1}01]$ zone axis of hcp α -Ti and the $[100]$ zone axis of bct Ti_2Cu . The diffraction peaks were overlapped between the two phases, indicating the presence of coherency between hcp α -Ti and bct Ti_2Cu . The $(\bar{1}011)$ planes of the hcp α -Ti phase are coherent with the $(0\bar{1}3)$ planes of the bct Ti_2Cu phase. This revealed that the propagation of the dislocations at the early stage of the deformation (Fig. 7(a)) and of the shear bands at the late stage of the deformation (Fig. 7(b) and (c)) were arrested at the boundaries of the Ti_2Cu phase. By combining the differences in microstructure and selected area diffraction pattern between the partially and fully deformed samples, one can suggest that the dislocations rotate the α -Ti phase at the early stage of the deformation towards forming a layered structure along the shear bands, which increases the amount of strain in the nanostructured matrix.

4. Discussion

4.1. Importance of the interfaces in the

$\text{Ti}_{66.1}\text{Nb}_{13.9}\text{Ni}_{4.8}\text{Cu}_8\text{Sn}_{7.2}$ nanostructure–dendrite composite

Based on the systematic investigations of the microstructural evolution upon deformation of the $\text{Ti}_{66.1}\text{Nb}_{13.9}\text{Ni}_{4.8}\text{Cu}_8\text{Sn}_{7.2}$ nanostructure–dendrite composite, we can suggest that the interfaces between the dendrites and the nanostructured matrix and between the α -Ti and Ti_2Cu phase in the matrix have great importance for controlling the high strength and ductility of the material. The nucleation of the shear bands occurs at the dendrite/matrix interfaces in order to accommodate the severe strains generated by the slip bands. This indicates that these interfaces should be structurally coherent to accommodate the initial shear stress. In the nanostructured matrix, the volume fraction of the α -Ti phase is much higher than that of the Ti_2Cu phase. Accordingly, similar to the typical duplex microstructure in conventional Ti alloys [22], the interfaces are generated by the β - and α -Ti solid solution phases with a strong structural coherency. When rotation of the dendrites occurs, such structural coherency between the β -Ti dendrites and α -Ti phase in the matrix can effectively compensate the tensile/compressive stresses by the local volume changes at the interfaces without cracking. Upon deformation the stability of the interfaces can also compensate the propagation of the shear bands, producing the extra stepped interfacial areas even in the fully deformed sample (Fig. 5).

The nanostructured matrix contains a mixture of soft hcp α -Ti (solid solution) and hard bct Ti_2Cu (intermetallic

compound) crystalline phases. The microstructural rearrangement to form the sandwich morphology is predominantly achieved by the elongation of the α -Ti grains along the direction of the dominant shear bands. Consequently, most shear bands can pass through the boundaries between the hcp α -Ti and bct Ti_2Cu phases. The bct Ti_2Cu phase in the sandwiched matrix is effective to reflect the shear bands, which propagate perpendicularly to the dominant shear bands. Consequently, the nature and arrangement of the phases in the nanostructured matrix is important to enhance the strength and ductility of the nanostructure–dendrite composite.

4.2. Rotational deformation in the dendrites

4.2.1. Generation of shear bands

Fine-scale slip bands without preferred orientation form in the dendrites, indicating the occurrence of homogeneous deformation at the early stage of compression, i.e. for the partially deformed $\text{Ti}_{66.1}\text{Nb}_{13.9}\text{Ni}_{4.8}\text{Cu}_8\text{Sn}_{7.2}$ nanostructure–dendrite composite sample. However, these profuse slip bands are arrested at the interface between the dendrite and the nanostructured matrix, as reflected by an uneven interfacial morphology. Such accommodation of the slip bands gives rise to a distribution of strains in the dendrites that is strongly inhomogeneous from the interfacial to the central areas of the dendrites. Furthermore, recent investigations on the microstructural evolution of the dendrites in the deformed and heat-treated $\text{Ti}_{66.1}\text{Nb}_{13.9}\text{Ni}_{4.8}\text{Cu}_8\text{Sn}_{7.2}$ revealed that a nanoscale ω phase locally precipitated only at the interfacial areas of the dendrites [23]. This also supports the inhomogeneous distribution of the strain in the deformed dendrites.

The observed deformation features and the origin of the shear bands can be related to grain boundary hardening [24]. Grain boundary hardening is postulated to be caused by dislocation forest hardening initiated from a free-length effect of the mobile screw segments or dislocation obstacles [24]. Due to the constraints imposed by the grain boundaries, slip also occurs on the less close-packed planes in regions near the grain boundary, which ultimately gives rise to a complex rotation of the lattice. In particular, the bcc structure of the β -Ti phase is not a close-packed structure and consequently slip occurs on several less close-packed planes such as $\{110\}$, $\{112\}$, and $\{123\}$ [24], resulting in the wrinkled/wavy features of slip bands on the specimen surface (Fig. 3), in order to nucleate the shear bands.

4.2.2. Propagation and interaction of the deformation bands in the dendrites

The shear bands nucleated at the dendrite/matrix interfaces propagate into the dendrites and the matrix. However, the propagation of the shear bands is arrested by the work-hardened dendrites, producing the pronounced stained contrast, as shown in Fig. 4(b). Furthermore, the width of the shear bands in the central areas of the dendrites is much

broader than that near the interfacial areas. This suggests that there is a gradual decrease of the shear strain when the shear bands pass through the dendrites from the interfacial to the central areas during the interaction with the work-hardened dendrites. Moreover, the inhomogeneous distribution of the accumulated strains in the dendrites may additionally help to arrest the propagation of the shear bands. Fig. 8 displays two simple schematic illustrations to describe the imbalance of the shear strains in the dendrites. If the distribution of the strains in the dendrites were homogeneous, there would be a perfect balance during the propagation of the shear bands, i.e. shear components, $\tau_1 = \tau_2$, as sketched in Fig. 8(a). In this case, the actual resistance to the propagation of the shear bands only depends on the intrinsic properties of the dendrites, e.g. the atomic bonding. In contrast, if the distribution of the strains is heterogeneous in the dendrites, as depicted in Fig. 8(b), there would be an imbalance in the shear components, $\tau_1 > \tau_2$. Such an imbalance of the shear components on the shear bands causes the rotation of the dendrites in order to release the shear strains. Furthermore, the imbalance of the shear stress in the dendrites can trigger the rotation of the nanostructured matrix, producing local volume changes at the interface with the dendrites. This is discussed in Section 4.3. The detailed microstructural investigations on the areas exhibiting interaction of the shear bands and the work-hardened dendrites (inset in Fig. 4(b)) reveal that new slip bands pass through the shear bands under an angle of $\sim 30^\circ$ to the previously formed slip bands in the work-hardened dendrites. This indicates that the accumulated strain in the work-hardened dendrites can be released in the partially deformed sample during the propagation of the shear bands. Therefore, the propagation of the shear bands in the inhomogeneously work-hardened dendrites firstly interacts with the previously formed slip bands, causing the imbalance of the shear strains. This imbalance of the shear strains initiates the rotation of the dendrites by releasing the accumulated strains and forming new slip bands in the dendrites.

In the present investigation, the formation of the ω phase with plate-like morphology has been observed along

the shear bands. Upon shock deformation [25] or thermal heat treatment [18], the formation of the ω phase has been reported for β -Ti and β -Zr supersaturated solid solutions containing bcc structure stabilizers (Cr, Mn, V, Nb, Mo, and Fe). Based on the lattice collapse model [26], the shock-induced ω phase formation has been explained by considering a specific habit plane that can offer a lower formation energy, thus leading to a plate-like morphology [25,26]. In contrast, the thermally induced ω phase forms with a spherical morphology without any preferred habit plane [18]. Consequently, it is clear that the ω phase formation mechanism itself can be judged from its morphology. Based on this understanding, one can suppose that the ω phase in the present investigation forms upon deformation due to its plate-like morphology. However, since shock deformation is generally considered to cause much higher localized strains than conventional compressive deformation, the ω phase formation mechanism observed in the present investigation should be different from the lattice collapse model.

In general, crystals with bcc and hcp structures have a restricted number of easy mobile slip bands compared to crystals with fcc structure [27]. Furthermore, the formation of partial dislocations can be strongly suppressed [27]. This indicates that the β -Ti dendrites in the $\text{Ti}_{66.1}\text{Nb}_{13.9}\text{Ni}_{4.8}\text{Cu}_8\text{Sn}_{7.2}$ nanostructure–dendrite composite have a preferred orientation for the propagation of slip bands, i.e. [111] on {110} planes. Therefore, the direction of the newly formed slip bands after the local rotation of the dendrites can be identical to the previous direction of the slip bands. In addition, it is known that the athermal $\beta \rightarrow \omega$ martensitic transformation in β -Ti alloys is diffusionless and reversible, and can be easily stress-induced [28]. In the partially deformed sample, it is inevitable to create a stress-concentrated area when the interaction occurs between the previously existing and the newly formed slip bands. As a result, transforming β into athermal ω phase is one possible way to release effectively the accumulated stress. The transformed ω phases might also become obstacles for the movement of subsequent slip bands, contributing to work hardening to some extent.

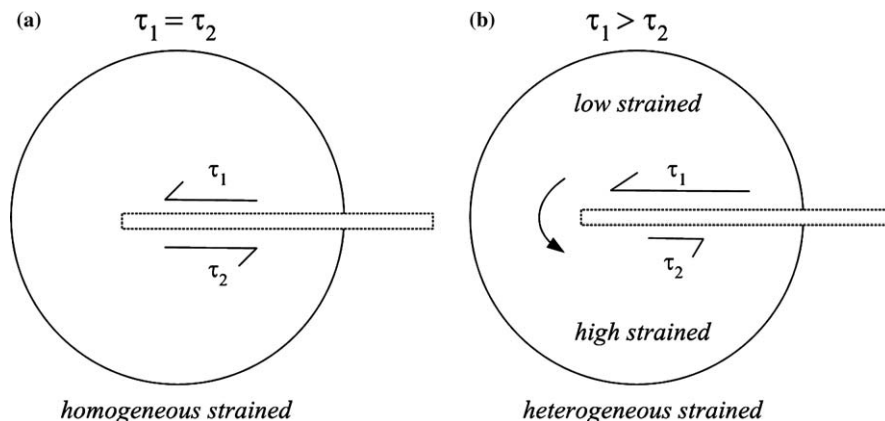


Fig. 8. Schematics to explain the rotation of the dendrites using the imbalance of the shear stress.

After further deformation, e.g. in the fully deformed sample, the dendrites contain a high density of shear bands. Moreover, the interaction of the shear bands occurs perpendicularly. Due to the strong contrast from the shear bands, it is difficult to find any slip bands, as shown in Fig. 5. Furthermore, the shear bands penetrate the interface between the dendrite and the nanostructured matrix, forming a stepped morphology. However, even after the propagation of the shear bands for full deformation, one can find moiré fringes in the dendrites as an evidence of the rotation of the dendrites [14]. This proves that the rotation of the dendrites has occurred in the fully deformed sample. By comparing the microstructures of the dendrites between the partially and fully deformed samples, the rotation of the dendrites in the fully deformed sample can be linked with the generation of the moiré fringes. This suggests that the degree of the rotation of the dendrites in the fully deformed sample is much larger than that in the partially deformed sample due to the high strains. This indicates that the deformation is dominated by the propagation of shear bands in the fully deformed sample.

In general, the propagation and interaction of shear bands in materials yields a plateau stress–strain curve [11]. However, if such propagation and interaction of shear bands are accompanied by a phase transformation, by which the accumulated mechanically introduced energy can be dissipated, further stress may be needed to propagate the shear bands. In this scenario, the reversible ω phase in the dendrites may firstly transform into α'' phase with increasing deformation, similar to the stress-induced phase transformation in Ti-based alloys [29,30]. Subsequently, the α'' phase transforms into the disordered β phase due to a shape memory effect [30]. Hence, the local distorted β phase in the present investigation can form by a transformation not of the ω phase but of the α'' phase.

4.3. Rotational deformation in the nanostructured matrix

The rotational deformation in the dendrites by the propagation of the shear bands leads to a local change of the volume, especially at the interfacial areas between the dendrites and the nanostructured matrix. Fig. 9 shows a schematic illustrating the occurrence of the local volume change by the rotation of the dendrites. Such local volume changes accompany the different local stress fields, as indicated in Fig. 9. The local volume change caused by the rotation of the dendrites will also affect the nanostructured matrix. As marked by circles in Fig. 9, the nanostructured matrix has to develop local tensile/compressive stresses to accommodate the volume changes. From the microstructural investigations, it is clear that the nanostructured matrix of the $\text{Ti}_{66.1}\text{Nb}_{13.9}\text{Ni}_{4.8}\text{Cu}_8\text{Sn}_{7.2}$ nanostructure–dendrite composite contains hcp α -Ti and bct Ti_2Cu phases. The hcp α -Ti phase surrounds the bct Ti_2Cu phase indicating that the volume fraction of the hcp α -Ti phase is larger than that of the bct Ti_2Cu phase. The interfacial areas of

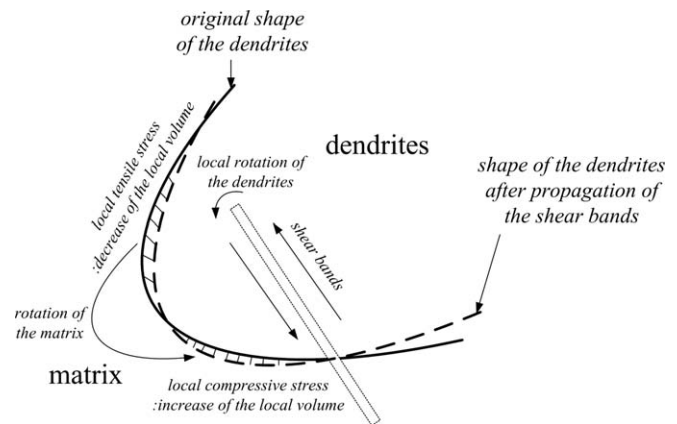


Fig. 9. Schematic of the local volume changes at the interfaces between the dendrites and the nanostructured matrix, and of the rotation of the nanostructured matrix.

the nanostructured matrix close to the dendrites face the hcp α -Ti phase instead of the bct Ti_2Cu phase. Consequently, the local tension/compression forces generated by the rotation of the dendrites can easily reach the hcp α -Ti phase. In general, a solid solution phase, e.g. the hcp α -Ti phase, is expected to be much softer than an intermetallic compound, e.g. the Ti_2Cu phase. This indicates that the dislocations easily form in the hcp α -Ti phase and are then arrested by the Ti_2Cu phase in the nanostructured matrix, as shown in Fig. 7. Moreover, the corresponding diffraction pattern in Fig. 7 reveals the rotation of the diffraction peaks from the hcp α -Ti phase in the nanostructured matrix, similar to the typical diffraction peaks from a textured microstructure. In contrast, the corresponding diffraction peaks from the bct Ti_2Cu phase are almost spherical, indicating that there is no significant deformation. This suggests that the local volume changes caused by the rotation of the dendrites induce deformation of the hcp α -Ti phase in the nanostructured matrix at the early stage of the deformation.

After further deformation, i.e. in the fully deformed sample, the microstructure of the nanostructured matrix contains a sandwich-like morphology between the hcp α -Ti and bct Ti_2Cu phases, which is well aligned along the shear bands. The sandwich-like morphology is arranged parallel to the steps formed by the propagation of the shear bands at the interfacial area between the dendrite and the nanostructured matrix. Apparently, the shear bands pass through the boundaries of the sandwich-like morphology in the nanostructured matrix. Hence, this sandwich-like morphology can effectively deflect the propagation of the shear bands, which pass through the nanostructured matrix perpendicularly, as shown in Fig. 7(c). This indicates that both hcp α -Ti and bct Ti_2Cu phases in the nanostructured matrix are significantly elongated following the direction of the main shear forces, leading to the formation of the sandwich-like morphology by rearranging the grains of the nanostructured matrix.

5. Summary

The microscopic deformation behavior of the $\text{Ti}_{66.1}\text{Nb}_{13.9}\text{Ni}_{4.8}\text{Cu}_8\text{Sn}_{7.2}$ nanostructure–dendrite composite has been investigated based on an analysis of the microstructural changes upon deformation. At the early stage of deformation, slip bands are homogeneously distributed in the dendrites and become arrested at the interfaces between the dendrites and the nanostructured matrix causing the work hardening of the material. The propagation of the shear bands is blocked inside the work-hardened dendrites showing a strong interaction between slip and shear bands. This arrest of the shear bands occurs not only by the interaction between the slip and shear bands but is also linked to the rotation of the dendrites, caused by the imbalance of the shear stress. The imbalance of the shear stress is initiated by the inhomogeneous distribution of the slip strain between the central and the interfacial areas of the dendrites. The propagation of the shear bands in the dendrites locally releases the accumulated strains along the shear bands, thus forming new slip bands with a different orientation from the previously formed slip bands. The interaction between previously and newly formed slip bands accompanies the transformation of the β -Ti phase into the ω phase with a plate-like morphology. After further deformation of the sample, one can only find amorphous and distorted β -Ti phases along the shear bands in the dendrites but the plate-like ω phase has disappeared.

In contrast, there is no mechanically induced phase transformation in the nanostructured matrix, consisting of a mixture of hcp α -Ti and bct Ti_2Cu phases. Instead, the microstructure of the matrix is rotated to compensate the local volume difference, which is caused by the rotation of the dendrites. After further deformation, the hcp α -Ti and bct Ti_2Cu phases in the matrix form a sandwich-like microstructure parallel to the direction of the shear bands, similar to that in multilayered structures. The sandwiched hcp α -Ti and bct Ti_2Cu microstructure is effective in releasing and reflecting the shear strains. Therefore, the nanostructured matrix mainly contributes to the overall strength of the $\text{Ti}_{66.1}\text{Nb}_{13.9}\text{Ni}_{4.8}\text{Cu}_8\text{Sn}_{7.2}$ nanostructure–dendrite composite but not so much to its ductility.

Acknowledgements

The authors thank F. Baier, G. He, M. Heilmaier, M. Kusy, G. Miehe, C. Müller, S. Scudino, R. Theissmann,

S. Venkataraman, P. Yu and W.Y. Zhang for technical assistance and stimulating discussions. Funding by the EU within the framework of the Research Training Network on ductile bulk metallic glass composites (MRTN-CT-2003-504692) is gratefully acknowledged. One of the authors (W.X.) greatly appreciates the financial support of the Alexander-von-Humboldt Foundation.

References

- [1] He G, Eckert J, Löser W, Schultz L. *Nat Mater* 2003;2:33.
- [2] He G, Eckert J, Löser W. *Acta Mater* 2003;51:5223.
- [3] He G, Eckert J, Löser W, Hagiwara M. *Acta Mater* 2004;52:3035.
- [4] Dai QL, Sun BB, Sui ML, He G, Li Y, Eckert J, Luo WK, Ma E. *J Mater Res* 2004;19:2557.
- [5] He G, Eckert J, Dai QL, Sui ML, Löser W, Hagiwara M, Ma E. *Biomaterials* 2003;24:511.
- [6] Das J, Löser W, Kühn U, Eckert J, Roy SK, Schultz L. *Appl Phys Lett* 2003;82:4690.
- [7] Das J, Güth A, Klauf H-J, Mickel C, Löser W, Eckert J, Roy SK, Schultz L. *Scripta Mater* 2003;49:1189.
- [8] He G, Hagiwara M, Eckert J, Löser W. *Philos Mag Lett* 2004;84:365.
- [9] Zhang ZF, He G, Eckert J. *Philos Mag* 2005;85:897.
- [10] Zhang ZF, He G, Zhang H, Eckert J. *Scripta Mater* 2005;52:945.
- [11] Zhang H, Pan XF, Zhang ZF, Das J, Kim KB, Müller C, Baier F, Kusy M, Gebert A, He G, Eckert J. *Z Metallkd* 2005;96:675.
- [12] Eckert J, Das J, Kim KB, Baier F, Löser W, Calin M, Zhang ZF, Gebert A. *J Alloys Compd* 2006; accepted for publication.
- [13] Kim KB, Das J, Baier F, Eckert J. *Appl Phys Lett* 2005;86:171909.
- [14] Kim KB, Das J, Baier F, Eckert J. *Appl Phys Lett* 2005;86:201909.
- [15] Kim KB, Das J, Baier F, Eckert J. *Phys Stat Sol (a)* 2005;202:2405.
- [16] PDF#34-0657, PCPDFWIN Version 2.2, JCPDS-International Centre for Diffraction Data, 2001.
- [17] Woodcock TG, Kusy M, Mato S, Alcalá G, Thomas J, Löser W, Gebert A, Eckert J, Schultz L. *Acta Mater* 2005;53:5141.
- [18] Shao G, Tsakirooulos P. *Acta Mater* 2000;48:3671.
- [19] Dawson CW, Sass SL. *Metall Trans* 1970;1:2225.
- [20] Williams DB, Carter BC. *Transmission electron microscopy: III. Imaging*. New York: Plenum Press; 1996. p. 444.
- [21] Son YI, Lee YK, Park KT, Lee CS, Shin DH. *Acta Mater* 2005;53:3125.
- [22] Blümke R, Müller C. *Z Metallkd* 2005;93:1119.
- [23] Kim KB, Xu W, Das J, Eckert J. Unpublished works.
- [24] Dieter GE. *Mechanical metallurgy*. SI metric edn. London: McGraw-Hill; 1988. p. 184.
- [25] Dey GK, Tewari R, Banerjee S, Jyoti G, Gupta SC, Joshi KD, Sikka SK. *Acta Mater* 2004;52:5243.
- [26] Hsiung LM, Lassila DH. *Scripta Mater* 1998;38:1371.
- [27] Massalski RB. *Physical metallurgy*, vol. 1. Amsterdam: North-Holland; 1996. p. 135.
- [28] De Fontaine D, Paton NE, Williams JC. *Acta Metall* 1971;19:1153.
- [29] Duerig TW, Albrecht J, Richter D, Fischer P. *Acta Metall* 1982;30:2161.
- [30] Baker C. *J Mater Sci* 1971;5:92.